Continuous Electrochemical Heat Engines

- Supplementary Materials -

Methods

- Decoupling κ, ρ, and α in continuous electrochemical heat engines
- Extended table of dV_{OC}/dT values
- Gas-phase $H_2/H_2O\|O_2$ demonstration
- Continuous liquid-phase $V^{2+/3+} \| Fe(CN)_6^{3-/4-}$ energy harvesting system, and the calculation of energy conversion efficiency as $\eta = 0.61\eta_c$.
- Thermophysical Properties of Liquid Couples
- System modeling and simulation

Tables S1 – S3

Figures S1 – S8

Decoupling of κ, ρ, and α in continuous electrochemical heat engines

We first discuss the optimization of electrical resistance R_{Lead} and heat flow Q_{Lead} via stacking for an electrochemical heat engine of total cell membrane area A_{cell} at each temperature. Wiedemann-Franz law states that for any one single-material conduit, the product $\kappa\rho$ is a function of temperature only. Consequently, heat (Q_{Lead}) and electrical (P_{Lead}) losses cannot be optimized simultaneously, with their product $P_{Lead}Q_{Lead}$ being only a function of temperature and current I. For the heat engine, like for a two-legged thermoelectric, the product $P_{Lead}Q_{Lead} = 4 (LT)I^2 \Delta T$, where LT is the expression of Wiedemann-Franz law. However, unlike a thermoelectric or thermogalvanic device, the electrochemical heat engine with a total cell area A_{cell} consists of stacks of N cells connected in series, each with area A_{cell}/N, and operates at finite current densities J to draw electrical power. For the electrochemical heat engine, $I = JA_{cell}/N$, and the quantity $P_{Lead}Q_{Lead}$ can be minimized by increasing N without otherwise affecting the power output of the overall device.

We now turn to the heat leaks along the working fluid. In the electrochemical heat engine, electrical charge can in principle flow between T_H and T_C via two parallel pathways: via the leads and via the working fluids (Figure 2a). In a thermogalvanic (or thermoelectric) system with only one such pathway across ΔT, $R_{Lead} \rightarrow \infty$ (i.e., it is electrically disconnected), R_{Fluid} (which refers in our case to the ionic transport of net charge) is both finite and constrained by the Wiedemann-Franz law, and the cell stack resistances (R_H, R_C) $\rightarrow 0$. In the electrochemical heat engine, $(R_H, R_C, R_{Lead}) << R_{Fluid}$, and $R_{Fluid} \rightarrow \infty$. The working fluid carries no net electrical current between T_H and T_C, even though it may contain ionic species. Thus the heat leak that is coupled to R_{Fluid} can in principle asymptotically approach zero without violating the Wiedemann-Franz law, which is accomplished in practice with a heat exchanger.

This allows to further minimize the conductive heat loss via the working fluid, nominally $\kappa_{Fluid}A_{HX}\Delta T/L_{HX}$, by making the heat exchanger sufficiently long, and by e.g. cutting off circulation and breaking thermal contact completely, which is not possible in a solid-state or thermogalvanic system. Notably, this does not affect the continuous operation of the electrochemical cells. It is important to note that since the electrical leads do not have to take the same dimensions as the heat exchanger, L_{HX} does not constrain the electrical resistance of the leads via Wiedemann-Franz law. In simulations, we have kept the two length dimensions equal for simplicity.

Furthermore, for scaled systems, we can introduce a parameter t_{on} to define the fraction of time that the working fluid is in thermal contact with both the hot and cold reservoirs. We can then operate the system such that $(1- \varepsilon_{HX})\ \dot{m}c_p\Delta T >> t_{on}(\kappa_{Fluid}A_{HX}\Delta T)/L_{HX}$. This is similar to the operation of thermally regenerative cycles which charge and discharge batteries isothermally between heating and cooling them.[1,2]

Extended table of dV_{OC}/dT values

The thermopower of many solution-phase electrochemical couples was measured before arriving at the $V^{2+/3+} \parallel Fe(CN)_6{}^{3-/4-}$ system. Their 'electrochemical Seebeck coefficients' are listed in Table S1. Couples denoted (1) were measured on carbon paper electrodes (SpectraCarb 2050a, heat treated at 400ºC in air for 30hrs prior to use) versus an isothermal Ag/AgCl reference electrode (Aldrich, 4M KCl) separated from the solution of interest by a 4M KCl salt bridge to minimize junction potentials. The temperature coefficient of the reference electrode was first calibrated by a thermal voltage measurement of two references, and found to be consistent with literature data for the Ag/AgCl couple [3,4]. Thermocouples (Omega type T) were coated with a thin layer polymethyl methyacrylate (PMMA, Aldrich) from a toluene solution (Aldrich) and attached directly to the electrodes. Temperature and voltage signals were collected with a data acquisition unit (Agilent 34972A). The thermopower of couples denoted (2) were measured on an activated carbon electrode (ELAT hydrophilic, functionalized as above) versus an isothermal Ag/AgCl reference electrode (CH Instruments) in a stirred cell. The temperature of the jacketed glass cell was maintained with a chiller with temperature deviations within 0.1 ºC, and measured with a K-type thermocouple protected by a PTFE sleeve. The data was collected with a BioLogic SP-240 potentiostat. The thermopower of $Fe^{2+/3+}$ (denoted 3) was obtained by measuring against the isothermal $Fe(CN)_6{}^{3-/4-}$ couple on carbon paper electrodes (SpectraCarb 2050a) which had been coated with a Pt-C catalyst ink consisting of 50µg/µL HISPEC 40%Pt on high surface area carbon in 3:2:0.1 H_2O (MilliQ Synergy UV) : Isopropanol (Aldrich) : Nafion 117 dispersion (Aldrich), dropcast onto the positive electrodes for a total Pt loading of 0.5mg/cm².

For two-couple dV_{OC}/dT measurements, the membrane-electrode assemblies were fabricated using carbon electrodes, Ti foil current collectors (GalliumSource, Grade II, 12.5µm thickness), Nafion perflourinated proton exchange membranes (Nafion 115, FuelCellStore, 127µm, or Nafion 212, 51µm, FuelCellStore), and silicone gaskets (McMaster-Carr, 500µm), and the electrode temperature was monitored using PMMA-coated thermocouples. The cross-sectional area of the circular carbon electrodes was 1.1cm², but the active electrode area was set by the through-hole in the silicone gasket at 0.95cm². All cells were filled with water and briefly placed under low vacuum for ~10 minutes before testing, to ensure that no air pockets remained inside

the porous carbon electrodes. The open-circuit voltage and temperature were measured at 0.5 second intervals with a digital acquisition unit (Agilent 34972A). Example raw data from this type of measurement is shown in Figure S4a. A deconstructed view of this type of cell is shown in Figure S4b. The temperature was monitored at the electrode surface as the entire cell was lowered into water baths at different temperatures, as shown in Figure S4c.

The $V^{2+/3+} \| Fe(CN)_6^{3-/4-}$ energy harvester was tested under constant N_2 purge in both electrode compartments. The negative electrode was fabricated using carbon cloth (ELAT hydrophilic, 400μm thickness), heat treated in air at 400ºC for 30hrs prior to the experiment to functionalize the electrode surface, as described previously [5]. The positive electrode was fabricated with a 0.5mg/cm^2 Pt loading on carbon paper (Spectracarb 2050a, 252μm thickness), as described above. The thicker (127μm) Nafion membrane was to prevent crossover between the vanadium and ferrocyanide electrolytes. Prior to testing both electrode compartments were filled with 3MVOSO$_4$ (Aldrich) in 6M HCl (Aldrich) in degassed water, 1mL in the negative electrode compartment and 3mL in the positive electrode compartment. A potential of 1.4V was then applied across the cell until 430 coulombs of charge had passed through the cell, such that the negative electrode compartment then contained a 1:1 mixture of V^{2+} and V^{3+}, and the positive electrode compartment contained a 1:1 mixture of V^{4+} and V^{5+} species. The positive electrode compartment was emptied with a syringe, rinsed with degassed water, and re-filled with 375mM $K_4Fe(CN)_6$ and 375mM $K_4Fe(CN)_6$ in degassed pH 7.2 phosphate buffer prior to testing. The positive electrode compartment was covered in aluminum foil due to the known sensitivity of ferrocyanide compounds to light [6]. The vanadium compartment was left open to monitor the blue-green-purple color change that confirms a successful reduction procedure.

In a scaled-up energy harvesting system, the circulation of electrolyte may result in a reduction of mass-transfer related overpotential, and correspondingly more favorable polarization behavior is expected. To gain insight into to the magnitude of the improvement that could be realized with fast flow outside of the membrane-electrode assembly, peristaltic pumps (ZJchao, 12V) were used to provide jet-impingement mass transfer enhancement inside both anolyte and catholyte chambers. The pump apparatus is visible above the cell in Figure S4c. The improvement in mass transfer behavior is shown in Figure S1.

Gas phase demonstration
We used anode-supported solid-oxide button fuel cells available commercially from Fuel Cell Materials (ASC2.0) and used without modification. The cells were sealed with molten Ag at approximately 920 °C in two Probostat testing rigs (Norwegian Electroceramics) shown in Figure S2. Each seal was monitored to yield no detectable leaks in a downstream bubbler at an overpressure of 2 cm of water for at least 5 minutes. The active area of each cell is 1.10 cm^2.

We controlled for microscopic gas leaks across the fuel cells by ensuring they have the same open-circuit potentials at the same temperatures. Measured open-circuit potentials were within 10 mV of the Nernstian limit. Over the course of the two-day experiment, we adjusted T_H down as the open-circuit potential degraded by ~3 mV to avoid artificially inflating the voltage and power density of the system. This resulted in a slight underestimation of the power density of the system.

The gas compositions supplied to the system were 5% H_2 balance Ar, humidified at a room temperature of 18 °C, versus dry 21% O_2 in Ar, both at flow rates of approximately 80 sccm as measured by mass flow controllers (MKS) calibrated with Ar.

At every temperature, at least 30 minutes was allowed for equilibration; the total operating time for the experiment was ~3 days. The J-V curve in Figure 4 was taken with a BioLogic SP-240 potentiostat in a 4-electrode configuration as a series of galvanostatic steps. In each step, the current was allowed to stabilize over 5 seconds, enough to reach a consistent steady-state value.

Continuous liquid-phase energy harvesting system, and the calculation of energy conversion efficiency as $\eta = 0.61\eta_c$.

$V^{2+/3+}$ || $Fe(CN)_6^{3-/4-}$ liquid flow cells were constructed as shown in Figure S5. Positive electrodes were made from carbon cloth (ELAT hydrophilic, 400μm thickness) that was first functionalized by burning in air for 30s using a butane torch. A Pt-C catalyst ink consisting of 50μg/μL HISPEC 40%Pt on high surface area carbon in 3:2:0.1 H_2O (MilliQ Synergy UV):Isopropanol (Aldrich):Nafion 117 dispersion (Aldrich) was dropcast onto the positive electrodes for a total Pt loading of 0.5mg/cm². Scanning electron micrographs of these electrodes are shown in Figure S5. Negative electrodes were made from carbon paper (Spectracarb 2050a, 252μm thickness) functionalized by burning in air for 30s using a butane torch. Electrode contacts were made with strips of Ti foil (GalliumSource, Grade II, 12.5μm thickness). Anolyte and catholyte flows were separated by a Nafion 212 membrane (FuelCellStore, 51μm thickness). The membrane-electrode assembly was compressed into a machined acrylic housing, and sealed using silicone rubber gasket sheeting (McMaster-Carr, 500μm in the negative electrode compartment, 1250μm in the positive electrode compartment). A channel cut into each gasket sheet (1cm x 10cm) defined the flow path through each cell.

A counterflow heat exchanger was constructed in a similar manner to the two flow cells, as shown in Figure S6. Two channels were cut in two separate silicone rubber gaskets (McMaster Carr, 120μm thickness). A strip of Ti foil (GalliumSource, Grade II, 12.5μm thickness) was placed between the two gaskets, and the foil-gasket assembly was compressed between machined acrylic sheets, forming a 2-channel counterflow heat exchanger. In the energy harvesting system, the $Fe(CN)_6^{3-/4-}$ electrolyte was run in one channel, and the $V^{2+/3+}$ electrolyte in another. This allowed matching of the flow rate and heat capacity of the hot-to-cold and cold-to-hot streams in each channel, so that a heat exchange effectiveness of 1 corresponded to a heat exchange efficiency of 100%. While this counterflow heat exchanger performed modestly at higher flow rates, as shown in Figure S6c, it clearly operated with a much lower effectiveness at the very low flow rates $\dot{m}$ used in the energy harvesting experiments. This poor performance at low flow rates is likely due to the balance between the exchanged heat flux and the heat loss to the ambient, which increases with the increasing residence time in the heat exchanger at low flow rates. At the low flow rates, the effective conductance of the flow of liquid of heat capacity c_p was relatively smaller than that due the convective loss to the ambient for the heat exchanger outer surface area A and convective heat transfer coefficient h. To mitigate this loss, future

energy harvesting systems for which $h A > (\dot{m} \, c_p)$ should be sealed and tested under low vacuum conditions.

All energy harvesting experiments were conducted in a N_2-purged glove box (MTI VGB-4 with Instru-Tech Stinger pressure regulator, MTI O_2 sensor and no H_2O regulation). For these experiments, two of the liquid flow cells were connected in a single fluidic circuit as shown in Figure S7. Two peristaltic pumps (Masterflex 77120-32) were driven at a low duty cycle as required to match the flow rate to the reaction rate. The flow rates at these pumps were calibrated prior to the tests by measuring the time required to fill a graduated cylinder. The flow rate of the $Fe(CN)_6^{3-/4-}$ electrolyte was 4x that of the $V^{2+/3+}$ electrolyte to compensate for the difference in charge capacity between the two solutions. One cell was placed in a chilled bath (Boekel Microcooler II, Model 260010) and the other in a temperature-controller water bath (Fisher Scientific 11-400-495HP). The cells were connected in series and electrical measurements were performed via galvanostatic techniques (Biologic SP-240, Current Scan technique). Temperature was monitored at both the hot and cold cells, and in at both liquid inputs to the hot cell using type thermocouples (Omega type T) that were welded with junction sizes <200μm (Omega TL-Weld) and coated with poly methacrylate (PMMA, Aldrich) cast from a acetone/toluene solution (Aldrich). This provided a very thin chemically-resistant coating that allowed the thermocouples to function despite the harsh chemical environment of the electrolyte. Temperature signals were collected using an analog signal processing unit (Agilent 34972A). Prior to use, the system comprising the peristaltic pumps, heat exchangers, and two flow cells was filled with the two electrolyte solutions. One solution contained 375mM Potassium Hexacyanoferrate (II) (Aldrich) and 375mM Potassium Ferricyanide (III) (Aldrich) in pH 7.2 phosphate buffer (Aldrich 94951) diluted 10:2 with deionized water (MilliQ Synergy UV). The other electrolyte was obtained by reduction of a solution containing 3M $VOSO_4$ (Aldrich) in 6M HCl (Aldrich) for ~40hrs in a vigorously stirred cell identical to that used for the dV_{OC}/dT measurements. An excess volume of 2M $VOSO_4$ (Aldrich) in 6M HCl (Aldrich) was oxidized at the counter electrode and discarded after use. The tubing of the energy harvesting system was disconnected directly upstream of the two peristaltic pumps, and the two electrolytes were slowly injected at the same time with two syringes as the pumps were run without the peristaltic rollers fully engaged. Both cells were oriented with inlets down during this process. Once the electrolyte volume was filled and electrolyte began to leak out of the disconnected tubing, the tubing was connected and the peristaltic rollers engaged. Extreme care had to be exercised when filling the system with the syringes, as excessive pressure in one syringe would rupture the membrane-electrode assembly separating the two electrolyte compartments in the upstream cell.

The effective power input to the energy harvesting system was estimated adding the thermodynamic heat input required by the electrode process $I*T_H \, (\alpha_1-\alpha_2)$ to the sensible heat leaked through the heat exchanger. This sensible heat leak was estimated by measuring the temperature increase of the electrolyte solutions as they traveled from the hot to cold cell, and multiplying the temperature increase ΔT of both solutions from the cold cell by the mass flow rate $\dot{m}$ and heat capacity c_p of each electrolyte solution. Ideally, the power input into the system would be calculated as $P_{in} = I*T_H \, (\alpha_1-\alpha_2) + [(\dot{m} \, c_p)_{FCN(II/III)}+ (\dot{m} \, c_p)_{V(II/III)}] \, (T_{Hot}-T_{Inlet})$, where T_{Inlet} is the measured temperature of both electrolyte solutions between the exits from the hot side of the heat exchanger and the inlets of the hot cell. However, temperature measurements at different points in the flow system indicated that the electrolyte circulation was slow enough that the electrolyte emerging from the cold cell nearly equilibrated with the glove box environmental

temperature (~28°C) before entering the heat exchanger. Since this heat transfer from the environment constituted an additional energy input, it was considered improper to measure the energy input in this way. As a result, for the purposes of the efficiency calculation, the energy input was calculated conservatively as $(I*V_{OC}) + [(\dot{m}\, c_p)_{FCN(II/III)} + (\dot{m}\, c_p)_{V(II/III)}]\, (T_{Hot}-T_{Cold})$. This energy input is much less than the total energy input from the heater, as the heat leaks through the cell leads and other heat loss to the environment. However, since it is equivalent to the energy input required in the complete absence of the heat exchanger, it is likely an upper bound on the energy input that would be required in a scaled up, insulated system. The c_p and density ρ values of both electrolytes were measured as described in the next section. The mass flow rate $\dot{m}$ was based on the measured densities ρ and the volumetric flow rates Q through the pumps, which had previously been calibrated using a graduated cylinder.

The power output from the energy harvesting system was obtained by measuring the system's current-voltage curve with a potentiostat (Biologic SP-240). The J-V curve was collected over the course of hours, with the flow rates matching electrical currents, and the system equilibrating between each point. Considerable degradation occurred on the timescale of the measurements. The resistance of the long (>2m) leads and contacts between the energy harvesting system inside the glove box and the potentiostat in the laboratory was measured between 1 and 1.5Ω, but this resistance was not compensated in the electrical measurement or the reported polarization curves because it varied slightly each time the leads were connected to the cell. The efficiency of energy conversion η was then calculated as:

$$\eta = \frac{Power\ output}{Power\ input} = \frac{Power\ output}{Thermodynamic\ heat\ input\ + heat\ leak} = $$
$$= \left(\frac{I*V}{I*T_{Hot}\left(\alpha_1 - \alpha_2\right) + \left(Q_{FCN} c_{p,FCN} \rho_{FCN} + Q_V c_{p,V} \rho_V\right)\left(T_{Hot} - T_{Cold}\right)} \right) \quad (1.2)$$

Here the subscript V denotes the $V^{2+/3+}$ electrolyte, and FCN denotes the $Fe(CN)_6^{3-/4-}$ electrolyte. This yielded the reported values of $\eta = 0.042$ (0.34 η_c) at 0.25mA cm^{-2} and $\eta = 0.018$ (0.15 η_c) at the maximum power point of 1.8mA cm^{-2} matched to the flow rates of 3.7 and 15 μl min^{-1} for a 10 cm^2 cell. For the flow rates employed in our experiments and simulations, the heat transferred by convection in the working fluids, $(1-\varepsilon_{HX})\, \dot{m}\, c_p \Delta T$, exceeds the possible conductive contributions $\kappa(\Delta T)A_{HX}/L_{HX}$ from a stagnant electrolyte, and therefore convection is the mode of heat leak in the working fluids, justifying the use of equation (1.2). The calculated components of power and heat flows are detailed in Table S3. These efficiency values do not include the impact of the heat exchanger, out of consideration for the leak of heat into the system from the ambient discussed above. We also exclude the conductive heat leaks along the walls of the heat exchanger, and along the current collecting leads, as well as pumping power (since our peristaltic pumps are oversized for the experimental flow rates). Nonetheless, it is interesting to project the efficiency of a scaled-up system, in which the flow rate of electrolyte could be increased such that the heat loss to the ambient due to long residence times in the heat exchanger could be minimized. In this case, the effective efficiency of the energy harvesting system could be estimated as:

$$\eta = \left(\cfrac{I*V}{I*T_{Hot}\left(\alpha_1 - \alpha_2\right) + \left(Q_{FCN}c_{p,FCN}\rho_{FCN}\left(1 - \varepsilon_{HX}(Q_{FCN})\right) + Q_V c_{p,V}\rho_V \left(1 - \varepsilon_{HX}(Q_V)\right)\right)\left(T_{Hot} - T_{Cold}\right)} \right) \quad (1.3)$$

Here $\varepsilon_{HX}(Q)$ denotes the efficiency of the heat exchanger as a function of flow rate Q, which is equivalent to the heat exchanger effectiveness in this case because the $\dot{m}\,c_p$ are matched in both electrolyte streams. For example, based on the performance of the heat exchanger given in Figure S6c, if the electrode area of both cells was increased by 1000x, such that flow rates reached ~1mL/min for the $V^{2+/3+}$ and ~4mL/min for the $Fe(CN)_6^{3-/4-}$ electrolytes, this yields and η = 0.076 (0.61 η_c) at 0.5 mA cm^{-2}. While this efficiency estimate neglects heat losses to the environment, heat losses through power leads, and pumping power, and is therefore less realistic than the projected power and efficiency metrics in the main text, it is informative to compare this efficiency with that used by previous authors. For example, Lee et al. [2] use the same approach to report a system efficiency of η = 0.067 for a Thermally Regenerative Electrochemical Cycle (TREC). However, it's worth noting that the purely presumed heat exchange efficiency of 50% in that work would require a multi-step regenerative process, rather than the simple counterflow heat exchange implemented here, since liquid counterflow heat exchange is not practicable for TREC systems using solid battery materials.

Thermophysical properties of liquid couples

The specific heat c_p of $V^{2+/3+}$ and $Fe(CN)_6^{3-/4-}$ (FCN) solutions were measured between 25 ℃ and 35℃ using a Differential Scanning Calorimeter (TA Instruments Q2000 DSC). The density ρ of solutions used in this work was obtained by weighing known volumes of each solution (Mettler-Toledo XS205 Precision Balance, Finpipette F1 micropipette). This calorimetric data is shown in Table S2.

System modeling and simulation

Electronic Operation of One Cell

The open-circuit voltage of the system is $V_{OC} = \left(\alpha_1 - \alpha_2\right)\left(T_H - T_C\right) = \alpha\,\Delta T$

Voltage V is solved as a function of current density J: $V(J) = V\left(\text{local } c_o, c_R\right) - 2\eta_{act}(J) - JR_\Omega$

The voltage is added in series for the cells in the stack. The open-circuit potential for one cell was taken as Nernstian, including concentration terms, and a temperature-dependent reference potential:

$$E = \frac{RT}{nF} \ln\left(\frac{c_O^2}{c_R^2}\right) + E^0 + \alpha\left(T - 298.15\right) \quad \text{* MERGEFORMAT (2.1)}$$

For the heat engine operating with two cells using the same redox couples, the non-equilibrium Nernst voltage simplifies to $V = E_C - E_H = V_{OC} + \frac{RT_C}{nF} \ln\left(\frac{c_{O,cold,local}^2}{c_{R,cold,local}^2}\right) - \frac{RT_H}{nF} \ln\left(\frac{c_{O,hot,local}^2}{c_{R,hot,local}^2}\right)$

Here, concentrations are squared to account for the two concentration ratios on the two sides of the membrane, and referenced to 1M. The symmetric nature of each cell, and only equal concentrations considered, warrant this simplification. The total temperature coefficient α of the system was used as a parameter. Notably, as the current density approaches the mass transport limit, the concentration term becomes large, and dominates the resulting voltage loss.

Activation overpotential is given by the Butler-Volmer equation:

$$\eta_{act}\left(J\right) = \frac{RT}{0.5\,nF} \sinh^{-1}\left(\frac{J}{2\,k_0 c_O^{0.5} c_R^{0.5} \exp\left(-\frac{E_{act}}{R}\left(\frac{1}{T} - \frac{1}{T_{ref}}\right)\right)}\right) \quad \text{* MERGEFORMAT (2.2)}$$

For the liquid cell, we used a symmetry factor of 0.5, activation energy of 50 kJ/mol, and referenced the values of k_0 to 1M concentrations at 273 K. Notably, the concentrations used are local at the electrode. The activation overpotential diverges as the current density approaches the limiting current density, and one of the concentrations approaches zero. For the gas cell, the exchange current density formalism was used, with reference values given below.

Ohmic resistance was taken as 1/3 of resistance values for 1M HBr, [7] and Nafion resistance [8] was used for a membrane of thickness 25 microns, independent of temperature. The thickness of the acid solution was taken as the minimum of h_c and 0.15 mm. The conductivity of an acid solution was modeled to increase with temperature as diffusion is enhanced with decreasing viscosity of the fluid.

Local Concentration and Mass Transport

In calculating the local concentrations, a plug flow was assumed in the cell. The limiting current is given analytically with a Taylor series solution. The dimensionless measure of mass transport giving the maximum reagent utilization is calculated as:

$$\gamma = \frac{2}{h_c\,Pe} \int_0^{L_c} \left(\sum_{n=0}^{terms} \exp\left(-\left(n+0.5\right)^2 \pi^2 \frac{t}{h\,Pe}\right) \right) dt \quad \text{* MERGEFORMAT (2.3)}$$

Note that the Peclet number varies with temperature for a constant volumetric flow rate, due to the temperature enhancement of diffusion. The factor γ was calculated individually for the hot and cold cells. The Taylor series was evaluated to 30 terms, giving a compromise between underestimating the limiting current density and computational complexity.

Limiting current was calculated from the total inlet flux and the factor γ:

$$J_{\lim} = \gamma h_c w_c c_{O,R,inlet} F \qquad \text{\\* MERGEFORMAT (2.4)}$$

The local concentrations at the electrodes are given as $c_{O,R,local} = c_{O,R,inlet}\left(1 \pm \dfrac{J}{J_{\lim}}\right)$, depending on whether the species is consumed or produced at the electrodes. As the current density approaches the calculated limit, one of the local concentrations becomes fully depleted (even though the flow of the reagents to the cell may not be completely consumed). This affects both the Nernstian potential term, and the activation overpotential.

For connecting two cells in series, outlet reagent fluxes are calculated trivially at the first cell (hot cell in this simulation), and are used as inlet fluxes for the other cell. Since the cells are always current-matched and operating in reverse of each other, the inlet fluxes to the first cell are recovered from the outlet fluxes of the second. This assumes complete mixing of the electrolyte in between the cells, so that the concentrations of active species at the inlets of all cells are homogeneous.

System Hydrodynamics

The heat conductivity, specific heat, and dynamic viscosity for the solution in the liquid cells were assumed identical to water and taken from tables for liquid water at atmospheric pressure. For gases, respective temperature-dependent values were taken for O_2, H_2O, and H_2. [9–13]

For binary mixtures of gases, e.g. H_2 and H_2O, the specific heat and density were taken as linear combinations of the respective constituent values, while the heat conductivity and viscosity were recalculated [14,15] for the mixtures. For gases, the partial pressures were used as proxies for the composition fractions (x_1, x_2).

Laminar flow regime was used for the majority of calculations, and the assumption verified by checking the Reynolds number. The heat exchanger was assumed to have a counter-flow configuration with straight concentric circular pipes. Dimensionless quantities were calculated at the mean temperature between hot and cold cells for each working fluid in a circular pipe:

$$\mathrm{Re} = \frac{\rho v_{lin} 2r}{\mu} \cdot \frac{\pi r^2}{\pi r^2} = \frac{2\,\rho v_{vol}}{\mu \pi r} \;,\; \mathrm{Pr} = \frac{\mu\,c_p}{\kappa} \;.$$

The average Nusselt numbers were calculated separately for the thermal entrance region and fully developed flows under the assumption of laminar flow. The length of the entrance region for establishing laminar flow is given as $L_{ER} = 0.06 \times Re \times 2r$. The Nusselt number was calculated

for the entrance region using the Sieder and Tate correlation [16] modifying the traditional Graetz solution [17], neglecting the temperature dependence of viscosity: $Nu_{ER} = 1.86 \sqrt[3]{\frac{2r\ Re\ Pr}{L_{ER}}}$

The length L_{ER} varied widely and was in general not negligible compared to the simulated heat exchanger lengths (0.5-10 m). The Nusselt number for the fully developed laminar flow regions outside of the entrance lengths was taken as 48/11.

The convective heat transfer coefficient was calculated as $h = \frac{\kappa Nu}{2r}$. This is equivalent to making the assumption that the convective "depletion" width is comparable to the radius of the pipe, which is reasonable for long pipes.

Heat Exchanger and Pump Work
The heat exchanger is modeled as a counter-flow heat exchanger.

The thermal resistance of the heat exchanger wall is given analytically [17]: $R_{wall} = \dfrac{\ln\left(\frac{r+t}{r}\right)}{2\pi\kappa_{wall}L_{HX}}$.

In general, the heat conductivity of the exchanger is given as:

$$UA = \frac{N}{\dfrac{1}{2\pi r_i L_{HX} h_i} + \dfrac{R_{F,i}}{2\pi r_i L_{HX}} + R_{wall} + \dfrac{R_{F,o}}{2\pi (r_i + t)L_{HX}} + \dfrac{1}{2\pi (r_i + t)L_{HX} h_o}} \qquad \text{* MERGEFORMAT (2.5)}$$

The five terms in the denominator correspond to heat transfer across the fluid layers, the fouling resistances, and across the pipe wall in each heat exchanger. *UA* was first taken as an input parameter, together with *N*, r_i, and *t*, for the particular temperature and working fluids of the simulation. Assuming fully developed flows, L_{HX} was calculated. *UA* was then re-calculated, accounting for entrance regions in the heat exchanger. For example, if the two entrance lengths were calculated to be 10% of L_{HX} each, then the final *UA* was comprised of 80% the input value for fully developed flows, and 20% using equation * MERGEFORMAT (2.5) with one of the coefficients *h* re-calculated as above for an entrance region. When varying the input *UA* value parametrically, the parameter *N* was varied conjointly, so the total length L_{HX} remained constant (Figure 5a, Figure S8).

In the number of thermal units formalism, [18,19] the heat exchanger efficiency is given as:

$$\varepsilon_{HX} = \frac{\frac{UA}{\dot{m}c_p}}{1 + \frac{UA}{\dot{m}c_p}} \qquad \text{* MERGEFORMAT (2.6)}$$

This expression is simplified for the constraint of matching heat flows in the two pipes of the heat exchanger, which was enforced in simulations. The conductive heat leak along the cross-sectional area of the walls of each of 2*N* heat exchanger tubes in the system is given as:

$$Q_{wall} = \frac{\kappa_{wall}\Delta T}{L_{HX}}\pi\left(\left(r_i+t\right)^2+\left(r_o+t\right)^2-r_i^2-r_o^2\right)$$

MERGEFORMAT (2.7)

Similarly, the conductive heat losses in the electrical leads are:

$$Q_{lead} = 2\frac{\kappa_{lead}\Delta T}{L_{HX}}\pi r_{lead}^2$$

The head pressure in each annular tube is given analytically [20] as:

$$\Delta P_{HX} = \frac{8v_{vol}\mu L_{HX}}{\pi\left(r_o^2-r_i^2\right)\left(r_o^2+r_i^2-\frac{r_o^2-r_i^2}{\ln\left(r_o/r_i\right)}\right)}$$

* MERGEFORMAT (2.8)

The head pressure in each cell chamber is $\Delta P_{cell} = \frac{3v_{vol}\mu L_c w_c}{2h_c}$. The head pressure scales directly with the total area of cells, and independent of the number of cells in a stack of a given total area. Overpressures built up in the pipe junctions and bends were ignored. Note that the flow rate v_{vol} in each tube or cell depends inversely on number of identical heat exchanger tubes N. Since fluid utilization rates were never close to unity at maximum power points, the performance of one heat exchanger was calculated, and then the result was doubled for the system. The total head pressure to be pumped is given as:

$$P_{head} = 2\left(\Delta P_{HX,i}+\Delta P_{HX,o}+2\Delta P_{cell}\right)$$

* MERGEFORMAT (2.9)

Heat Engine Efficiency

For the liquid cell, the pumping was assumed to be mechanical: $P_{pump} = \frac{1}{\varepsilon_{pump}}v_{vol}P_{head}$. For the gas cell, pumping was assumed to be electrical at 20% efficiency: $P_{pump} = \frac{\rho RT v_{vol}}{\varepsilon_{pump}MW}\ln\left(\frac{P_{head}+P}{P}\right)$

The operating pressure P of the cells was taken as 1 atm. The density was calculated from STP values via the ideal gas law at the midpoint temperature of the system.
The power dissipated to the resistance of the electrical leads is a function of the total system current. With the simulations parametrized by J and the total cell area A held constant as the number of cells in a stack, N_{cells}, is varied, $I = JA/N_{cells}$. The power dissipated in leads is given as:

$$P_{lead} = I^2 R_{lead} = \frac{2\rho_L L_{HX}}{\pi r_{lead}^2}\left(\frac{JA}{N_{cells}}\right)^2$$

* MERGEFORMAT (2.10)

This term is the main origin of the scaling behavior of the system upon stacking. The resistance of mechanical components holding the stack together (i.e. bipolar plates) is ignored.

The power output of the system is

$$P_{system} = IV - P_{lead} - P_{pump} \qquad \backslash* \text{ MERGEFORMAT (2.11)}$$

The reversible entropy change for the electrochemical reaction at the hot side is:

$$\Delta S = \sum S_{prod} - \sum S_{react} \qquad \backslash* \text{ MERGEFORMAT (2.12)}$$

This has two components: the configurational concentration term, equivalent to the Nernstian concentration ratio, and the thermodynamic term. The thermodynamic term is the total effective thermopower α divided by the electron charge q. The reversible heat input to the system is $Q_{rev} = T_H \Delta S = I(\alpha_1 - \alpha_2) T_H$.

Phenomenologically, [2,21] the total heat input to the system is given as for a thermoelectric with a heat exchanger: $Q_{total} = \left(\alpha_1 - \alpha_2\right) I T_H + 2Q_{wall} + 2Q_{lead} + \left(1 - \varepsilon_{HX}\right)\left(\dot{m}c_p\right)_{total} \Delta T - 0.5 P_{lead}$

The efficiency of the system is $\eta_{system} = P/Q_{total}$, equivalent to equation (1) in the main text.

Maximum Power Point
For each set of design parameters (heat exchanger size, cell dimensions, stack size), and materials parameters (ohmic resistances, exchange current densities), the current density was swept to find the maximum power density. For the liquid system, the circulation flow rate was also left free during the optimization via the *Pe* number.

Constants and Parameters – Gas Cells
Total area 1 m^2, 100 cells, each 10 cm long and 10 cm wide, with chamber height 1cm. For the redox couples, a mixture of 10% H_2 and 90% H_2O versus 21% O_2 were used, for a thermopower of –0.42 mV/K. Using this mixture of gases in our experiment would have increased the power densities in Figure 4f by a factor of 1.93.

Electrolyte ohmic resistance: modeled as doped ceria with area-specific resistance (ASR) 0.1 Ω cm^2 at 500 °C, and activation energy 57 kJ/mol. Additionally, a 100 nm layer of YSZ was modeled. [22]

Activation overpotentials: hot cell at T_H with $j_{00} = 500$ mA cm^{-2} at 700 °C and activation energy 100 kJ/mol for the cathode and the anode. For the cold cell at T_C, $j_{00} = 150$ mA cm^{-2} at 500 °C, and activation energy 96.65 kJ/mol. Reference pressures $pH_2 = 0.97$ atm, $pH_2O = 0.03$ atm, and $pO_2 = 0.21$ atm were used, with unity pressure dependences for the anode, and square-root pressure dependences for the cathode.

Heat exchangers were modeled with silica heat conductivity, number of tubes $N = 50$, each with wall thickness 2 mm, inner radius 2 cm, and outer radius 4 cm, and conductivity for fully developed flows $UA = 20$ W K^{-1}. Leads were modeled as molybdenum, radius 1 cm, and with the same length as the heat exchanger.

Constants and Parameters – Liquid Cells

Total area 1 m^2, 100 cells, each 10 cm long and 10 cm wide, with chamber height 0.2 mm. All thermohydraulic parameters were taken as for liquid water. The diffusion coefficient of active species in the fluid at room temperature was taken as $D = 10^{-5}$ cm^2 sec^{-1}.

Heat exchangers were modeled with titanium heat conductivity, conductivity for fully developed flows $UA = 400$ kW K^{-1}, wall thickness 0.25 mm, inner radius 0.25 cm, and outer radius 0.5 cm, with a number of tubes $N = 10000$. Leads were modeled as molybdenum, with cross-section area 50 mm^2, and with the same length as the heat exchanger.

References

1.   Yang, Y. *et al.* Membrane-Free Battery for Harvesting Low-Grade Thermal Energy. *Nano Lett.* **14,** 6578–6583 (2014).

2.   Lee, S. W. *et al.* An electrochemical system for efficiently harvesting low-grade heat energy. *Nat. Commun.* **5,** 3942 (2014).

3.   DeBethune, A. J., Licht, T. S. & Swendeman, N. The Temperature Coefficients of Electrode Potentials: The Isothermal and Thermal Coefficients, The Standard Ionic Entropy of Electrochemical Transport of the Hydrogen Ion. *J. Electrochem. Soc.* **106,** 616–625 (1959).

4.   Bratsch, S. G. Standard Electrode Potentials and Temperature Coefficients in Water at 298.15K. *J. Phys. Chem. Ref. Data* **18,** 1 (1989).

5.   Sun, B. & Skyllas-Kazacos, M. Modification of graphite electrode materials for vanadium redox flow battery application-I. Thermal treatment. *Electrochim. Acta* **37,** 1253–1260 (1992).

6.   Hu, R. *et al.* Harvesting waste thermal energy using a carbon-nanotube-based thermo-electrochemical cell. *Nano Lett.* **10,** 838–46 (2010).

7.   Lide, D. *Handbook of Chemistry and Physics.* (CRC Press, 2012).

8.   Weber, A. Z. *et al.* Redox flow batteries: A review. *J. Appl. Electrochem.* **41,** 1137–1164 (2011).

9.   Saxena, S. & Saxena, V. Thermal conductivity data for hydrogen and deuterium in the range 100-1100 C. *J. Phys. A Gen. Phys.* **309,** (1970).

10.   Zykov, N., Sevast'yanov, R. & Voroshilova, K. Transport Properties of Nitrogen, Oxygen, Carbon Dioxide, and Air at Low Densities and Temperatures from 50 to 3000 K. *J. Eng. Phys.* **43,** 762–765 (1982).

11.   Beaton, C. *Heat Exchanger Design Fundamentals.* (1986).

12.   Assael, M. J., Mixafendi, S. & Wakeham, W. A. The Viscosity and Thermal Conductivity of Normal Hydrogen in the Limit of Zero Density. *J. Phys. Chem. Ref. Data* **15,** 1315–

1322 (1986).

13. Barin, I. *Thermochemical Data of Pure Substances*. (VCH, 1995).

14. Lindsay, A. L. & Bromley, L. A. Thermal Conductivity of Gas Mixtures. *Ind. Eng. Chem.* **42,** 1508–1511 (1950).

15. Wilke, C. R. A Viscosity Equation for Gas Mixtures. *J. Chem. Phys.* **18,** 517 (1950).

16. Sieder, E. N. & Tate, G. E. Heat Transfer and Pressure Drop of Liquids in Tubes. *Ind. Eng. Chem.* **28,** 1429–1435 (1936).

17. Incropera, F. & DeWitt, D. *Fundamentals of Heat and Mass Transfer*. (John Wiley & Sons, 2007).

18. Kakac, S., Bergles, A. & Mayinger, F. in *Heat Exchangers: Thermal-Hydraulic Fundamentals and Design* (1982).

19. Shah, R. K. & Sekulic, D. P. in *Fundamentals of Heat Exchanger Design* 735–808 (2003).

20. White, F. M. *Fluid Mechanics*. (2011).

21. Heikes, R. R. & Ure, R. W. *Thermoelectricity: Science and Engineering*. (Interscience Publishers, 1961).

22. Ni, M., Leung, M. K. H. & Leung, D. Y. C. Parametric study of solid oxide fuel cell performance. *Energy Convers. Manag.* **48,** 1525–1535 (2007).

Table S1 | Temperature coefficients of electrochemical couples. Raw data from this kind of measurement are shown in Figure S4a.

Couple	dV_{OC}/dT (mV/K)	Solution	Temperature Range (ºC)	Method
Fe(CN)$_6^{3-/4-}$	-1.4	200mM $K_4Fe(CN)_6$, 200mM $K_3Fe(CN)_6$, 100mM total KH$_2$PO$_4$/NaOH buffer	25-45	(1)
Fe(CN)$_6^{3-/4-}$	-1.3	400mM $K_4Fe(CN)_6$, 400mM $K_3Fe(CN)_6$	25-45	(1)
Fe$^{2+/3+}$	1.1	750mM FeCl$_2$, 750mM FeCl$_3$, 3M HCl	25-45	(3)
Fe$^{2+/3+}$	1.0	1.5M FeCl$_2$, 1.5M FeCl$_3$, 3M HCl	25-45	(3)
Benzoquinone/hydroquinone (BQ/HQ)	-1.1	10mM BQ, 10mM HQ, pH 7 PO_4 buffer 1M ionic strength	10-30	(2)
Benzoquinone/hydroquinone (BQ/HQ)	-0.9	10mM BQ, 10mM HQ, pH 4.5 PO_4 buffer 1M ionic strength	10-30	(2)
Benzoquinone/hydroquinone (BQ/HQ)	-0.6	10mM BQ, 10mM HQ, pH 2 PO_4 buffer 1M ionic strength	10-30	(2)
Benzoquinone/hydroquinone (BQ/HQ)	-0.3	10mM BQ, 10mM HQ, pH 1 PO_4 buffer 1M ionic strength	10-30	(2)
V(IV/V)	-0.1	100mM V(II/III) 2.1M SO$_4^-$	25-45	(1)
HBr/Br$_2$	0.2	500mM HBr	25-40	(1)
Methyl viologen$^{2+/+}$	0.6	10mM each, pH 7 PO_4 buffer 1M ionic strength	15-30	(2)
H$_2$/H+	0.8	500mM HCl	25-45	(1)
V(II/III)	1.2	2M V(II/III) 4M SO_4^{2-}	25-45	(1)
V(II/III)	1.2	3M V(II/III) 3M SO_4^{2-}, 6M Cl-	25-45	(1)
V(II/III)	1.6	100mM V(II/III), 100mM SO_4^{2-}, 6M Cl-	25-45	(1)
V(II/III)	1.7	100mM V(II/III) 2.1M SO_4^{2-}	25-45	(1)

Table S2 | Thermophysical properties of the aqueous electrolyte solutions used for the liquid phase energy harvesters.

Solution	ρ (kg m^{-3})	C_p (J g^{-1}K^{-1})
800mM Fe(CN)$_6^{3-/4-}$	1160	3.1
750mM Fe(CN)$_6^{3-/4-}$, .65M KH$_2$PO$_4$, 0.32M NaOH	1210	3.0
2M V$^{2+/3+}$, 4M SO$_4^{2-}$	1290	3.0
3M V$^{2+/3+}$, 3M SO$_4^2$, 6M Cl$^-$	1290	2.9

Table S3 | Components of the estimated efficiency of $0.15\eta_C$ at maximum power point for the liquid-phase continuous electrochemical heat engine.

Component	Value	Inputs
Electrical power output	1.1 mW	60 mV, 1.79 mA cm^{-2}, 10 cm^2
$I(\alpha_1-\alpha_2)T_H$	15.0 mW	2.6 mV K^{-1}, 17.9 mA, 323 K
$(\dot{m}\,c_p)_{FCN}\,\Delta T$	36.3 mW	15 µl min^{-1}, 40 K, Table S2
$(\dot{m}\,c_p)_V\,\Delta T$	9.2 mW	3.7 µl min^{-1}, 40 K, Table S2
Q along heat exchanger wall	NA	Not calculated
Q along current leads	NA	Not calculated
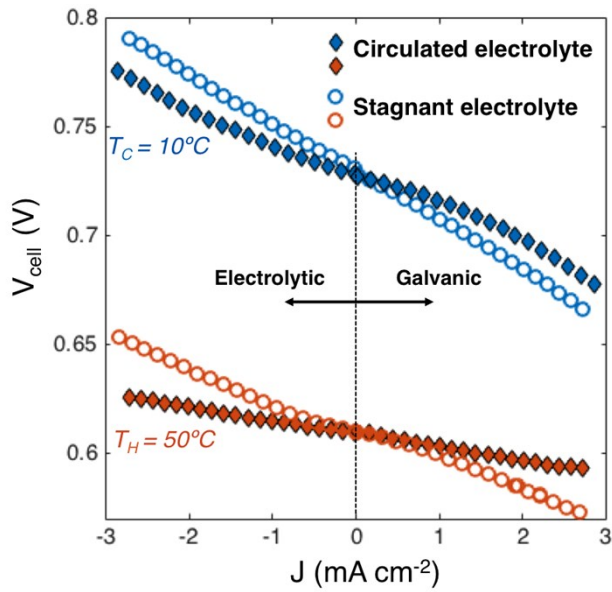
Figure S1 | The effect of jet-impingement fluid circulation on the polarization profile of the $V^{2+/3+} \| Fe(CN)_6^{3-/4-}$ energy harvesting system illustrating different temperature-dependencies of kinetic and transport-based overpotentials.
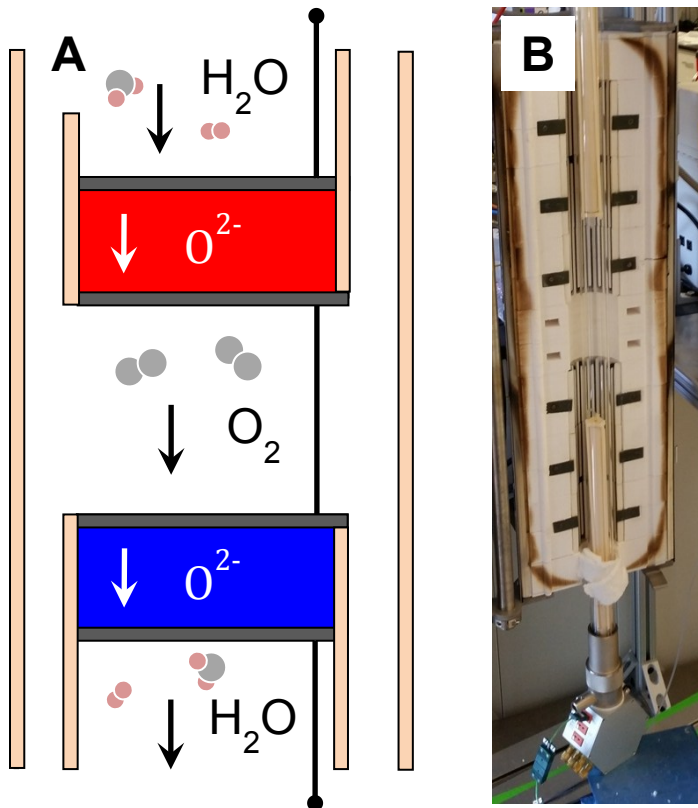

Figure S2 | gas-based electrochemical heat engine. a, schematic of the two-cell experimental setup for measuring heat harvesting with solid-oxide fuel cells. The red and the blue are oxygen-transporting membranes at T_H and T_C, connected electrically in series. **b**, Photo of the two-zone

vertical furnace used for the measurement with the two Probostat testing stations in a common quartz tube.
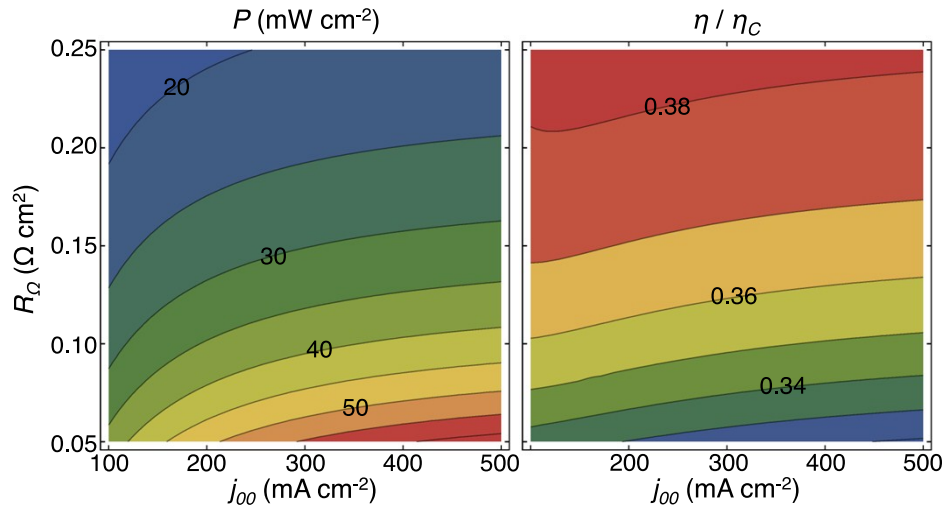
Figure S3 | Power output and efficiency as functions of R_Ω and j_{00} of the cold cell for a gas-phase continuous electrochemical heat engine. The reference values on the axes are given at 500 °C. Operation between $T_H = 900$ °C and $T_C = 500$ °C is shown. The parameters of the hot cell are not changed.
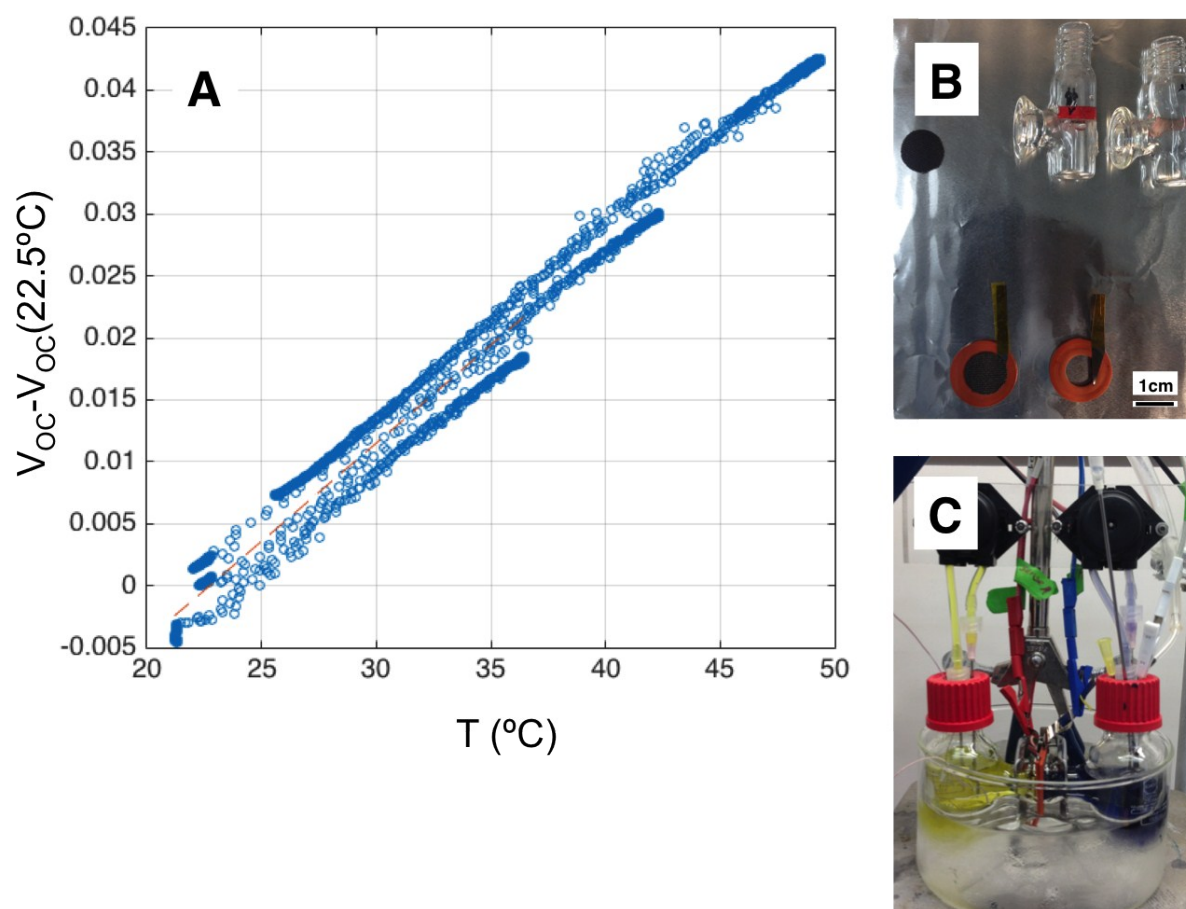
Figure S4 | Measurements of dV_OC/dT. a, Raw dV_{OC}/dT data obtained using the cell depicted in **b** disassembled. **c**, assembled membrane electrode assembly type cell engaged in dV_{OC}/dT measurements for the $V^{2+/3+} \parallel Fe(CN)_6^{3-/4-}$ system.

Within the figure, the following labels appear:

A

B

V^{2+} $2[Fe(CN)_6]^{4-}$

V^{3+} $2[Fe(CN)_6]^{3-}$

Leads

Gasket

Membrane

Electrodes

Thermocouples

C   50μm

D   1μm

E   500nm
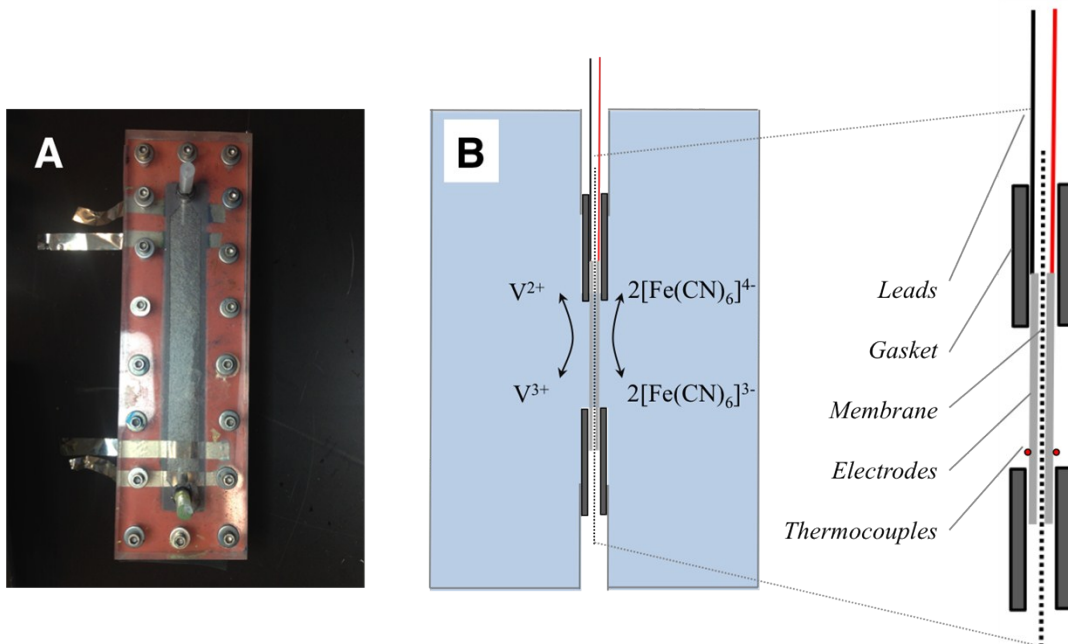
Figure S5 | Experimental cell for liquid-phase energy harvesting. a, the membrane electrode assembly flow cell used for liquid phase energy harvesting, somewhat worse for the wear after a round of testing. **b**, cross sectional view. **c – e**, scanning electron micrographs of the carbon paper electrodes with Pt/C catalyst coating that were used as the positive electrode.
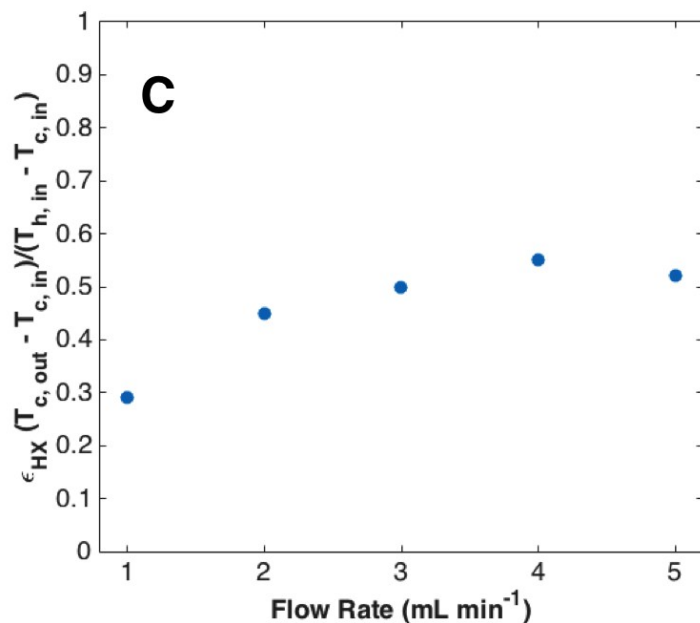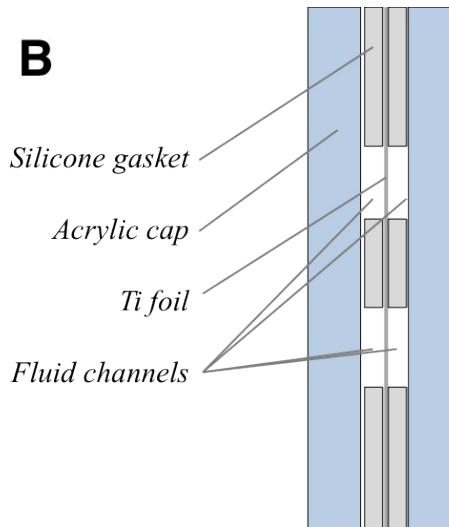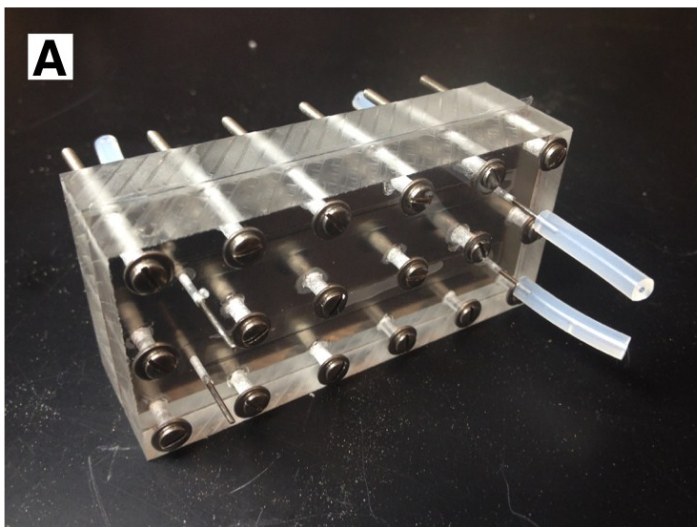
Figure S6 | Counterflow heat exchanger. a, 2-channel counterflow heat exchanger used in the energy harvesting experiments. **b**, cross-sectional view. **c**, performance of the heat exchanger in **a** at various flow rates.
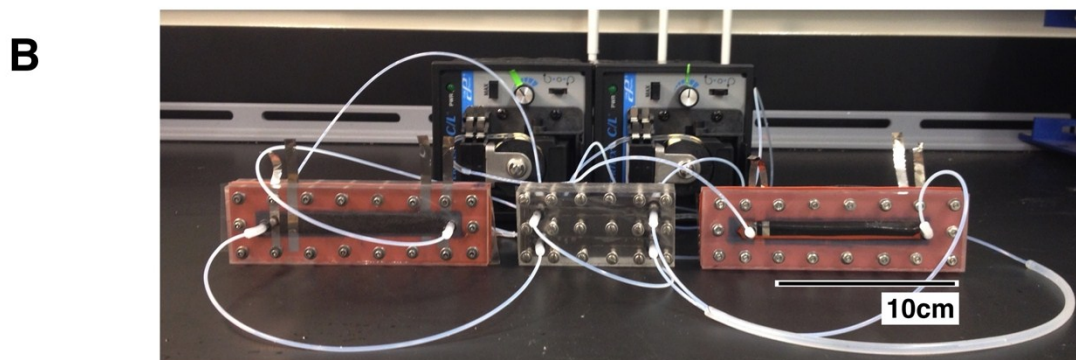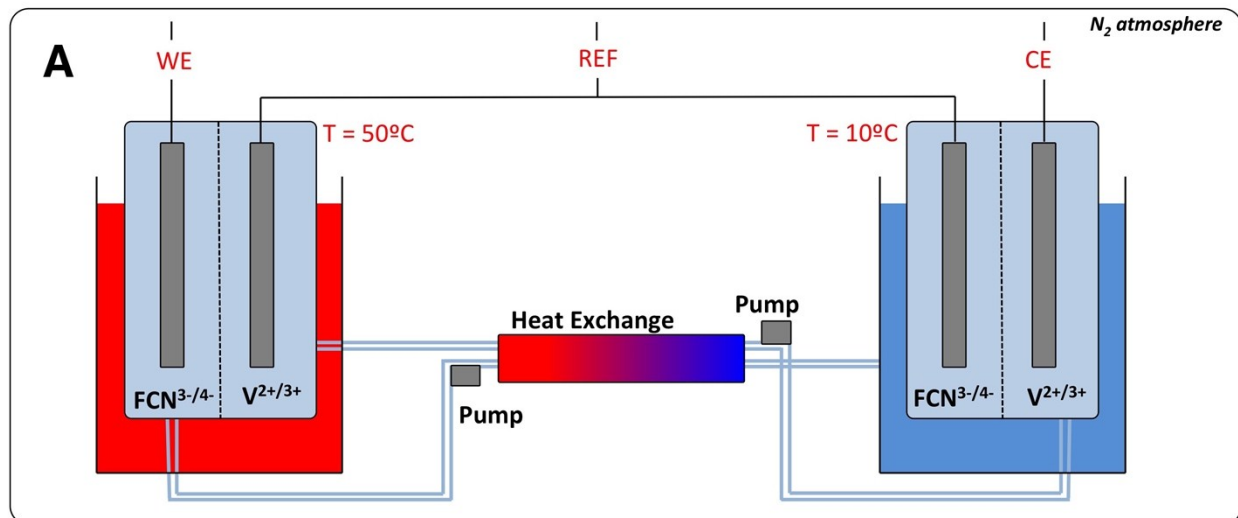
Figure S7 | Liquid-based continuous electrochemical heat engine. a, schematic and **b** photo of the liquid phase energy harvesting system before re-assembly in the glove box. "WE", "REF", and "CE" are the working, reference, and counter electrode connections to the potentiostat, respectively.
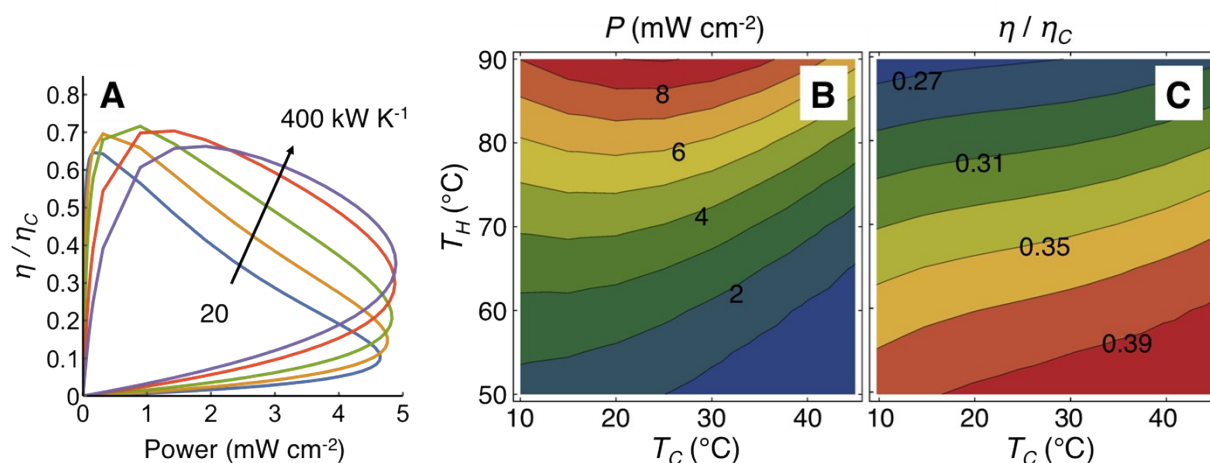
Figure S8 | Simulations of the liquid-based heat engine. a, efficiency vs. output power density for a liquid-based electrochemical heat engine operating between 50 °C and 10 °C, with heat exchanger *UA* 20, 50, 100, 200, and 400 kW K^{-1}, operating on electrolytes with total $\alpha = 3$ mV/K and concentrations 3M and 0.75M. **b**, power output, and **c**, efficiency as functions of T_H and T_C for a liquid-phase electrochemical heat engine with $\alpha = 3$ mV K^{-1} and $k_0 = 10^{-3}$ cm sec^{-1} and heat exchanger thermal conductivity 400 kW K^{-1}.